Estimation of phase function from diffuse reflectance images by deep convolutional neural networks

Yuxuan Liang[1], Chuang Niu[2], Chen Wei[3], Shenghan Ren[3], Wenxiang Cong[2] and Ge Wang[2]‡

[1] School of Physical Sciences, University of Science and Technology of China, Hefei, Anhui 230026, China

[2] Biomedical Imaging Center, Center for Biotechnology & Interdisciplinary Studies, Department of Biomedical Engineering, Rensselaer Polytechnic Institute, Troy, NY 12180, USA

[3] School of Electronic Engineering, Xidian University, Xi'an, Shaanxi 710071, China

E-mail: `wangg6@rpi.edu` (Ge Wang)

Abstract. The phase function plays an important factor in light propagation models especially for Monte Carlo (MC) simulation, which is usually represented by an empirical function with unknown parameters. In recent years, there have been some studies using machine learning methods to estimate the parameters of phase functions, but to our knowledge, no studies have attempted to estimate their form directly. We propose an inverse MC model based on convolutional neural networks to directly estimate the form of the phase function from diffuse reflectance images. A Gaussian mixture model-based phase function representation scheme is presented, which does not significantly increase the free parameters and provides the analytic expression of phase function to facilitate deflection angle sampling in MC simulations. The proposed method is validated on MC-simulated reflectance images of typical biological tissues using the Henyey-Greenstein phase function with different anisotropy factors. The best mean squared error of the phase function is 0.010 and the best relative error of the anisotropy factor is 3.280%. The effects of field of view (FOV) and spatial resolution are analyzed. The results suggest that the learning task becomes more difficult when using a larger FOV or higher resolution, and may require a more elaborate network model design and more training data.

Keywords: Light propagation, Phase function, Monte Carlo simulation, Convolutional neural networks, Field of view, Spatial resolution

1. Introduction

Knowledge of the optical properties of biological tissues is essential for developing diagnostic and prognostic applications of optical technologies. The commonly used

‡ Author to whom any correspondence should be addressed.

optical properties to characterize a tissue include the absorption coefficient (u_a), reduced scattering coefficient (μ'_s), scattering coefficient (u_s), scattering phase function $(p(\theta, \psi)$ where θ is the deflection angle of scatter and ψ the azimuthal angle of scatter), or scattering anisotropy (g), and the tissue refractive index (n) (Jacques; 2013). Since optical parameters are directly related to the structural and biochemical properties of tissues, their quantification provides important contextual information about the physiological state of the tissue (Calabro and Bigio; 2014). Depending on the categorization principle, techniques for measuring tissue optical properties can be divided into *in vitro* and *in vivo*, or direct and indirect methods, each with its own advantages and limitations (Wilson; 1995). The direct methods are limited to optically thin samples that typically require complicate preparation procedures. The indirect methods estimate the optical parameters by solving the inverse problem of a light propagation model. Since it is not limited to thin samples, indirect methods have better practical and nondestructive applications, for example, evaluation of kidney transplant viability (Rowland et al.; 2019) and tissue damage (Hokr and Bixler; 2021).

For indirect measurement methods, the widely used light propagation models include various analytic approximations of the radiative transfer model (Ishimaru; 1978), such as diffusion approximation equation (Wang and Wu; 2007), simplified spherical harmonics equations (Klose and Larsen; 2006), or hybrid models (Chen et al.; 2016); and Monte Carlo (MC) simulation (Wang et al.; 1995). Both types of methods usually adopt an iterative procedure to estimate the optical parameters or light deposition in tissues. Despite the huge computational burden, MC simulation is not limited (at least theoretically) with respect to the geometrical configuration of the experiments and the range of the determined optical properties (Yaroslavsky et al.; 1999), as such it has become the gold standard for studying the light propagation in biological tissues (Periyasamy and Pramanik; 2017).

When performing MC simulations, a prerequisite is the *a priori* information about the phase function, which describes the probability distribution for light to be deflected into different scattering angles at each scattering interaction (Bodenschatz et al.; 2015). Since direct measurement of the phase function using a goniophotometer is limited to thin samples and is particularly difficult for media with high anisotropy factor (Yaroslavsky et al.; 1999), the analytic approximations of phase function are more appealing in biomedical studies. Many approximate phase functions have been proposed in the literature, such as Henyey-Greenstein (HG) (Henyey and Greenstein; 1941), modified Henyey-Greenstein (Bevilacqua and Depeursinge; 1999) and Gegenbauer kernel (Yaroslavsky et al.; 1999). Among them, the heuristic HG function, although proposed 80 years ago, is still the most commonly used in MC software (Wang et al.; 1995; Fang and Boas; 2009; Ren et al.; 2013) because of the availability of its analytic inverse cumulative distribution function (CDF) greatly facilitates the sampling of deflection angles. However, the validity and accuracy of these phase functions in practical applications depend heavily on tissue characteristics and experimental conditions, as demonstrated in (Naglič et al.; 2019). Due to the optically heterogeneous nature of

biological tissues, the selection of phase function and the estimation of its parameters remains a difficult task, especially when the tissue geometry is complex.

In the past few years, the explosive advances in artificial intelligence, especially deep learning, have revolutionized many areas of research such as computer vision and natural language processing (Bengio et al.; 2021), tomographic imaging (Wang et al.; 2020), and, of course, photonics (Goda et al.; 2020). Specifically for the problem of tissue optical parameter estimation, Ivančič et al. (2018) proposed a neural-network-based model to estimate μ_a, μ'_s and two subdiffusive parameters (γ and δ) separately from subdiffusive spatially resolved reflectance, where the simulated observations of optical fiber probe were directly fed into a regression network consisting of three fully connected (FC) layers. Similarly, Zhao et al. (2018) and Sun et al. (2021) also employed FC networks, but with more layers to estimate μ_a and μ'_s using simulated frequency spatial domain imaging data. In Hokr and Bixler (2021), the moments of the profiles of spatial-temporal diffuse reflectance were used to estimate μ_a, μ'_s and n simultaneously using a four-layer FC network.

Although the aforementioned works have employed machine learning methods, none of them have explored the feasibility of estimating the form of the phase function. Motivated by the observation that the analytic approximations of phase function with a few free parameters may not be accurate enough to quantify the *in vivo* scattering characteristics in real experiments, this study attempts to estimate the phase function directly from the diffuse reflectance images using two-dimensional convolutional neural networks (CNN). Preliminary experiments were conducted on MC simulations of 11 typical biological tissues using a modified graphics processing units (GPU)-accelerated MC software CUDAMCML (Alerstam et al.; 2008), which is based on the pioneering work on steady-state MC simulation for multi-layered turbid media, MCML (Wang et al.; 1995). Whereas the experiments were performed in continuous wave (CW) mode, the proposed method can in principle be easily extended to other imaging modes, such as spatial-temporal and spatial-frequency domains.

Our main contributions can be summarized as follows. (1) We propose, to the best of our knowledge, the first data-driven CNN-based inverse MC model to directly estimate the scattering phase function from diffuse reflectance images. (2) We propose a Gaussian mixture model (GMM) to approximate the phase function, which does not significantly increase the free parameters and can provide the analytic expression of phase function to facilitate deflection angle sampling in MC simulations. (3) We investigate the effects of field of view (FOV) and spatial resolution on the accuracy of phase function estimation and give some suggestions that should take into account when applying CNN in phase function and other optical parameter estimation.

Table 1. Absorption and reduced scattering coefficients of the tissues.

Tissue	μ_a (cm^{-1})	μ_s' (cm^{-1})	Scattering category
Adipose	0.038	12.077	high
Bone	0.603	24.953	high
Bowel	0.117	11.490	high
Heart wall	0.583	9.639	high
Kidneys	0.654	22.530	high
Liver and spleen	3.490	6.781	low
Lung	1.948	21.739	high
Muscle	0.863	4.291	low
Skin	0.699	22.190	high
Stomach wall	0.113	14.369	high
Whole blood	11.621	18.140	low

2. Materials and methods

2.1. Biological tissues

Since this study focuses on the estimation of the form of phase function, we employ 11 typical biological tissues in the MC simulations, fixing μ_a and μ_s' while varying the g value of the anisotropy factor. This choice is made in consideration of the fact that existing techniques are more robust for the measurement of μ_a and μ_s', but less reliable for μ_s and g due to the diffusive nature of most biological tissues (Jacques; 2013). The μ_a and μ_s' values of the selected tissues are calculated based on the empirical functions and parameters provided in Alexandrakis et al. (2005). The photon wavelength is chosen to be 670 nm and the resulting absorption and reduced scattering coefficients are shown in Table 1. Based on the classification criteria and empirical thresholds summarized in Chen et al. (2016), the tissues are classified into high scattering and low scattering categories. Among the 11 tissues, liver and spleen, muscle and whole blood are the low scattering tissues, while the others are high scattering.

When generating the simulation data, the scattering coefficient μ_s required by CUDAMCML is calculated as $\mu_s = \mu_s'/(1-g)$ for a given value of g. The selection of g values is introduced in Section 2.5. The use of anisotropy factor g implies that the phase function is the HG function, which is the only type of phase function supported by CUDAMCML and most existing MC software including MCML (Wang et al.; 1995), MCX (Fang and Boas; 2009) and MOSE (Ren et al.; 2013). However, this is not a problem for validating the research objective of this study. Considering the generalization capability of machine learning methods, cross-validation of multiple types of phase functions is a problem worth investigating, but it is not addressed in this study.

2.2. MC simulation

The diffuse reflectance images of tissues are simulated using CUDAMCML (Alerstam et al.; 2008), a GPU-accelerated implementation of MCML (Wang et al.; 1995). Since MCML uses a Cartesian coordinate system to trace photon packets, but uses a cylindrical coordinate system to record the diffuse reflectance, we modify CUDAMCML to record the Cartesian position of photon packets as they hit the tissue surface to generate reflectance images in the xy-plane. The spatial resolution Δr in the radial direction is adopted as the resolution of the xy-plane. The size of the reflectance image $W \times H$ (in pixels) is determined by the total number of grid elements N_r in the radial direction, i.e., $W = H = 2N_r + 1$. In this way, we avoid the trouble of changing the input file format of MCML. As in the original implementation, photon packets hitting outside the FOV of $W \times H$ are recorded in the outermost rows or columns, but they are trimmed off when the images are fed into the neural network. For simplicity, the FOVs of the reflectance images are reported as $2N_r\Delta r \times 2N_r\Delta r$ in the followings. The modified CUDAMCML is build with CUDA 11.1 under Xubuntu 18.04.

2.3. Phase function representation

Estimating the phase function using neural networks is basically a regression problem that can be formulated as

$$p(\theta, \psi) = f(I_R(\mu_a, \mu_s, g)), \tag{1}$$

where I_R is the reflectance image generated by MC simulation and f is the nonlinear feedforward mapping function of the neural network acting as an inverse MC model. In thicker tissues where multiple scattering occurs, such as the semi-infinite tissues used in this study, it is valid to express the scattering phase function $p(\theta, \psi)$ as a function of the polar angle θ while omitting the dependence on the azimuthal angle ψ (Jacques; 2013; Bodenschatz et al.; 2016).

The popular heuristic HG function is defined as

$$p(\theta) = \frac{1}{4\pi} \frac{1 - g^2}{(1 + g^2 - 2g\cos(\theta))^{3/2}}, \tag{2}$$

where the anisotropy factor g is defined as the average cosine of the scattering angle, i.e., $g = \langle cos(\theta) \rangle$. Since the integral of $p'(\theta) = 2\pi p(\theta)\sin(\theta)$ over π is unity, the normalized HG function $p'(\theta)$ is used in the followings. For simplicity, it is still denoted as $p(\theta)$. In practical MC implementations, Equation 2 is written as a function of $\mu = cos(\theta)$:

$$p(\mu) = \frac{1}{2} \frac{1 - g^2}{(1 + g^2 - 2g\mu)^{3/2}}, \tag{3}$$

which facilitates the sampling of deflection angle at each scattering interaction from the analytic inverse CDF of $p(\mu)$ (Wang et al.; 1995).

Unlike existing studies that estimate the unknown parameters of a known form of the phase function, the goal of this study is to use a neural network to estimate an unknown form of the phase function based on the reflectance images. An intuitive

approach is to use $p(\theta)$ or $p(\mu)$ as the target for the neural network to learn from the training data. However, this leads to two problems. One is the number of discretizations of θ or μ, which will act as the number of neurons in the output layer of the neural network. Too few discretized grids will lead to large fitting errors, while too many discretized grids will result in excessive parameters to represent the phase function. Another problem is that when the discretized phase function representation is used for MC simulations, numerical sampling methods, such as the lookup table-based methods (Naglič et al.; 2017), are required, but these methods are computationally and memory intensive.

Considering the above issues, we propose to employ an analytic representation, the widely used Gaussian mixture models (GMM), to fit the unknown phase function. A GMM is defined as the superposition of some basic Gaussian densities of the form

$$p_{GMM}(x) = \sum_{k=1}^{K} \pi_k \mathcal{N}(x|m_k, \sigma_k), \tag{4}$$

where π_k, m_k and σ_k are the mixing coefficient, mean and variance of the kth Gaussian density $\mathcal{N}(x|m_k, \sigma_k)$, respectively, and K is the number of Gaussian components (NoG). The mixing coefficients must satisfy the requirements of $0 \le \pi_k \le 1$ and $\sum_{k=1}^{K} \pi_k = 1$. By using a sufficient number of Gaussian components with suitable parameters and suitable mixing coefficients, GMM can approximate almost any continuous density with arbitrary accuracy (Bishop; 2006).
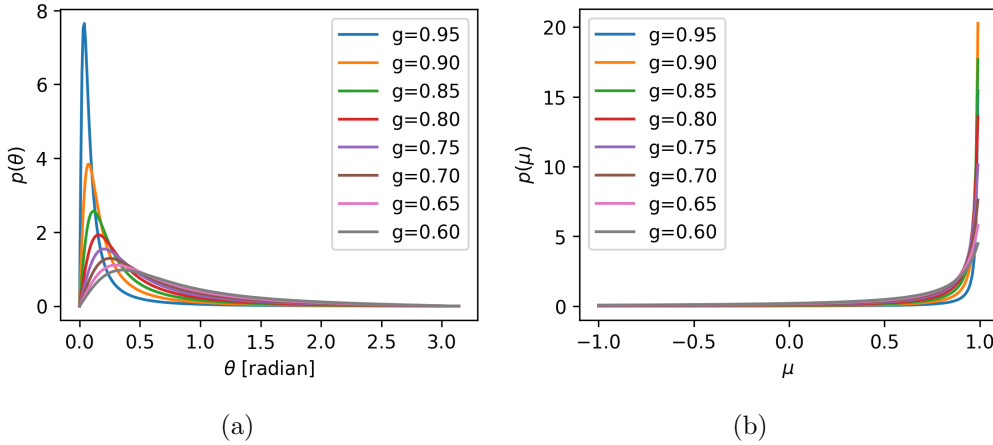

Figure 1. Chart showing the HG function with different anisotropy factors. (a) $p'(\theta)$. (b) $p(\mu)$.

Specifically for the phase function estimation problem, the independent variable x in Equation 4 has two choices, θ or $\mu = \cos(\theta)$. Figure 1 shows plots of $p(\theta)$ and $p(\mu)$ with the g values used in the experiments. Due to the symmetry of the basic Gaussian density, the asymmetric form of $p(\mu)$ makes it difficult to be approximated by GMM. For this reason, we choose the normalized HG function $p(\theta)$ as the target function for neural

network to regression. From Figure 1(a), it can be seen that the larger the anisotropy factor g, the narrower and steeper the HG function. Therefore, for large g values, it will be more difficult to fit the HG function using GMM, as will be demonstrated in the experiments.

2.4. Neural network model

Several factors should be taken into consideration when designing a neural network model to estimate the phase function. These include:

Network architecture: As a preliminary validation study, we directly adopt the off-the-shelf ResNet-18 model (He et al.; 2016) without spending any effort on the network architecture design. The original ResNet-18 model is modified to apply to the phase function regression problem as follows: (1) The channel number of the first layer is changed to 1 to accommodate the single-channel reflection images. (2) The number of neurons in the last FC layer is set to 3 times that of NoG, corresponding to π_k, m_k and σ_k for the K Gaussian components. (3) A sigmod layer is appended after the FC layer to normalize the outputs to the range [0, 1]. For ease of description, we will refer to the modified network model as PhaseNet.

Loss function: Two kinds of loss functions, the mean squared error (MSE) and Kullback-Leibler divergence between $p(\theta)$ and $p_{GMM}(\theta)$, were experimentally compared, and the results did not differ significantly. Since MSE is easier to understand, it is adopted to train and evaluate the PhaseNet. When calculating the loss function, θ is discretized into 1000 grids in the experiments. Because $p(\theta)$ is strictly defined in the interval $[0, \pi]$, but $p_{GMM}(\theta)$ is not, $p_{GMM}(\theta)$ is truncated to $[0, \pi]$ and normalized before the MSE is calculated. From $p_{GMM}(\theta)$, the anisotropy factor g can be estimated as

$$\hat{g} = \int_{\theta=0}^{\pi} p_{GMM}(\theta) \cos(\theta). \tag{5}$$

Model selection: Since the backbone of PhaseNet is fixed as ResNet-18, the NoG becomes the key parameter to determine the PhaseNet architecture. The optimal NoG for a given training dataset can be determined by using cross-validation or some analytic criterion such as the Akaike information criterion (AIC) or Bayesian information criterion (BIC) (Bishop; 2006). However, we find in our experiments that both AIC and BIC tends to favor overly simple models with the minimal test NoG value. This is due to the fact that AIC and BIC introduce a penalty term for the number of model parameters. In the PhaseNet, the number of free parameters in the FC layer is $512 \times (3 \times \text{NoG} + 1)$, where 512 is the number of output channels of the global pooling layer in ResNet-18. Therefore, the increase of the NoG leads to a significant increase of the FC layer parameters, which is discouraged by the AIC and BIC. Because of this reason, this study choose cross-validation for model selection.

The commonly used k-fold cross-validation scheme randomly divides a dataset into k mutually exclusive folds and then repeatedly selects one fold as the validation set and the remaining k-1 folds as the training set. This random sampling strategy is not

Table 2. Parameters of the reflectance image datasets.

Name	FOV (mm^2)	Resolution (Δr, mm)	N_r	Image Size	NoG
DS_1	2×2	0.02	50	99×99	11*
DS_2	4×4	0.02	100	199×199	11*
DS_3	6×6	0.02	150	299×299	11*
DS_4	4×4	0.01	200	399×399	11*
DS_5	4×4	0.04	50	99×99	11*

$\star$ Determined by leave-one-g-out cross-validation.
* Adopt the same value as DS_2.

effective in estimating the optimal NoG value, as demonstrated by our experiments, where the validation error has the same declining trend as the training error as the NoG increases. As a result, the maximal test NoG value is always recommended. We believe that this is caused by the similarity between the reflectance images with the same parameters. Although they are generated by running MC simulations independently, they have a high similarity due to the large number of photons used. Therefore, the validation set generated by randomly splitting the entire dataset cannot reveal the generalization ability of the model.

On the basis of the above trial-and-error experimental results, we finally employ a leave-one-g-out (LOGO) cross-validation method to determine the optimal NoG for PhaseNet. The LOGO cross-validation divides the entire dataset into training and validation sets according to the g values of the reflectance images. During each iteration of cross-validation, images with one g value are used as the validation set, while the remaining images with other g values are used for training.

2.5. Experimental setup

Five reflectance image datasets are constructed to investigate the effects of FOV and spatial resolution on the estimation accuracy of the phase function. The details of the datasets are presented in Table 2. All 11 tissues are used for all the datasets, and each dataset has its own training and test subsets. The diffuse reflectance images of the tissues are simulated separately by CUDAMCML using a semi-infinite slab geometry and an infinitely narrow incident photon beam with 10 million photons. The thickness of the tissues is set to 100 cm to ensure the semi-infinite assumption.

In typical biological tissues, the anisotropy factor g ranges between 0.7 and 0.99 (Cheong et al.; 1990). In our experiments, the lower bound of g is set to 0.6 to introduce a larger variance in the phase functions. Specifically, for each tissue, g varies from 0.65 to 0.95 with a step size of 0.1 for the training data, and varies from 0.6 to 0.9 with a step size of 0.1 for the test data. For each parameter set (μ_a, μ_s and g), 200 samples for training and 40 samples for test are generated. The total numbers of images for training and test in each dataset are 8800 and 1760, respectively.

The optimal NoG value for each dataset can be determined individually by LOGO

Table 3. Overview of the results.

Dataset (FOV)	MSE	Gain (%)	Relative Error of g (%)
DS_1 (2×2@0.02)	0.012 ± 0.016	-16.7	3.421 ± 4.426
DS_2 (4×4@0.02)	0.010 ± 0.013	–	3.280 ± 3.047
DS_3 (6×6@0.02)	0.017 ± 0.013	-41.2	3.910 ± 3.450
DS_4 (4×4@0.01)	0.029 ± 0.022	-65.5	5.232 ± 5.302
DS_5 (4×4@0.04)	0.011 ± 0.016	-9.1	3.151 ± 3.263

cross-validation. However, in order to fairly compare the performance of PhaseNet on different datasets, we want to keep all factors except for FOV and resolution as consistent as possible. Therefore, the optimal NoG value of DS_2, which has the moderate FOV and spatial resolution, is applied to all other datasets. The optimal NoG for DS_2 is 11, determined by varying the NoG from 2 to 12.

After obtaining the optimal NoG, the PhaseNet models are trained on each dataset separately using all the training data. Due to the stochastic nature of the training process of neural network models, five models are trained on each dataset respectively.

3. Experimental results

3.1. Implementation details

The proposed PhaseNet is implemented with Pytorch 1.8.2 on a single NVIDIA GeForce RTX 3090 graphics card. During LOGO cross-validation and training stages, the models are trained with momentum SGD optimizer for 30 epochs with a momentum of 0.9 and a weight decay of 0.005. A step-wise learning rate decay scheduler is used with an initial learning rate of 0.005, step size of 10 epochs, and drop rate of 0.1. The batch size is 220 for all datasets. The commonly used horizontal and vertical flipping are utilized for data augmentation. At test stage, the five PhaseNet models for each dataset are tested on the corresponding test data separately and their estimation errors (MSE) are averaged. The code of PhaseNet is publicly available at `https://github.com/liangyuxuan1/phasefunction2`.

3.2. Overview of results

Table 3 presents an overview of the experimental results. For simplicity, the units of FOV (mm^2) and spatial resolution (mm) are omitted here and below, and an FOV is denoted together with the spatial resolution when necessary as, e.g., 4×4@0.02. The MSE is averaged over all tissues and anisotropy factors for each dataset. The gain of performance is defined as the relative error in percentage between the MSE of the reference dataset DS_2 and that of other datasets. The minus symbol represents performance degradation. The relative error of g is defined as $(|g - \hat{g}|/g) \times 100\%$.

As seen in Table 3, the best estimation accuracy is achieved on DS_2

(FOV=4×4@0.02). Using the performance on DS_2 as a reference, the performance gain on other datasets is calculated. Reducing the FOV to 2×2 (DS_1) or expanding it to 6×6 (DS_3), while maintaining the resolution of 0.02, results in 16.7% and 41.2% drop in accuracy, respectively. When keeping the FOV unchanged but increasing the resolution to 0.01 (DS_4) or decreasing it to 0.04 (DS_5), the estimation error increases by 65.5% and 9.1%, respectively. The relative error of g has a similar trend as the MSE.

(a)

(b)
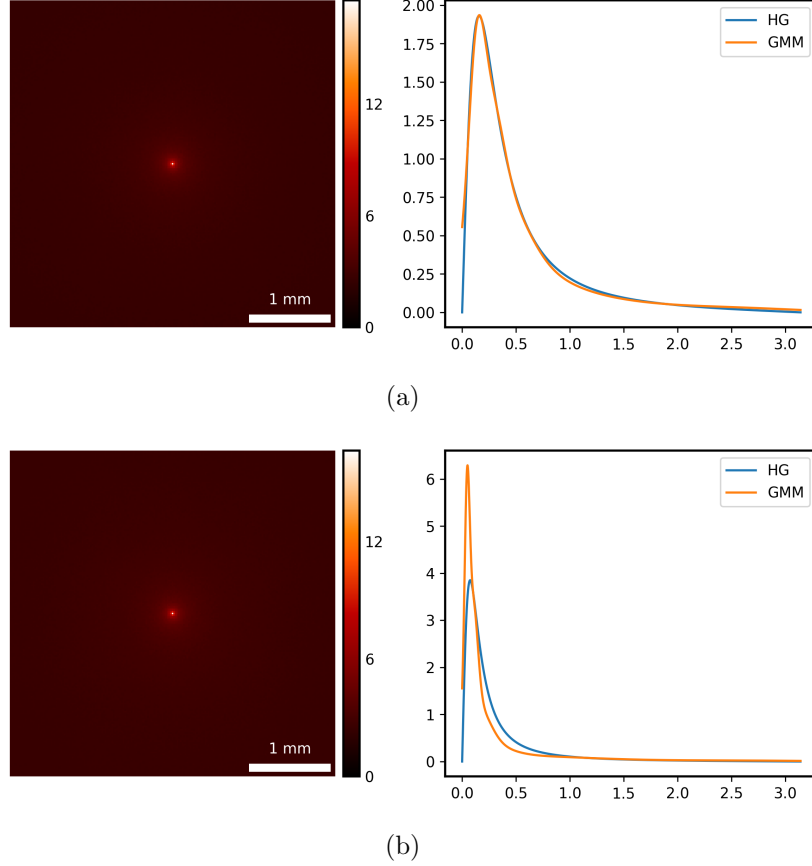
Figure 2. Example results. (a) Example with small estimation error. Tissue: heart, $u_a = 0.583$ cm^{-1}, $u_s = 48.194$ cm^{-1}, $g = 0.80$, MSE=0.002. (b) Example with large estimation error. Tissue: heart, $u_a = 0.583$ cm^{-1}, $u_s = 96.387$ cm^{-1}, $g = 0.90$, MSE=0.136. The dynamic range of the reflectance images on the left is compressed by Gamma transformation ($\gamma = 0.5$) for visualization. FOV=4×4@0.02 for both images. The ground truth HG function and the estimated GMM are on the right. The x-axis of the phase function is θ, in radian.

The MSE values do not provide an intuitive sense of how close the estimated phase functions are to the ground truth. However, the nonlinear nature of phase function estimation (regression) prevents us from using the R-squared statistic to evaluate the fit of the PhaseNet models. Therefore, we visually inspect the experimental results. Figure 2 show two example images with the smallest and largest estimation error in DS_2. In both examples, the reflectance images look very similar despite the different tissue parameters of μ_s and g. The PhaseNet does capture the basic form of the HG

phase function, but apparently it has difficulties at the boundary of $\theta = 0$ and at large g value of 0.9 where the phase function is much steeper and narrower.

3.3. Effect of FOV on estimation accuracy

The MSE of the phase functions estimated by the PhaseNet models on DS_1, DS_2 and DS_3 are shown in Figure 3. These datasets have different FOVs but have the same spatial resolution of 0.02. At first glance, the larger the FOV, the larger the estimation error. In order to quantify the statistical differences, the Wilcoxon rank sum test is used to test the differences in MSE across FOVs at each g value separately because the estimation errors are not normally distributed ($p < 0.05$, Shapiro-Wilk test). The results indicate that the MSEs are significantly different ($p < 0.05$) at all g values except for that of FOV 2×2 (blue dot) versus 6×6 (purple dot) at g=0.9. The error plots for FOV 2×2 and 4×4 cross each other, but the average error of FOV 4×4 is smaller. The estimation error of FOV 6×6 is significantly larger than the other two FOVs.
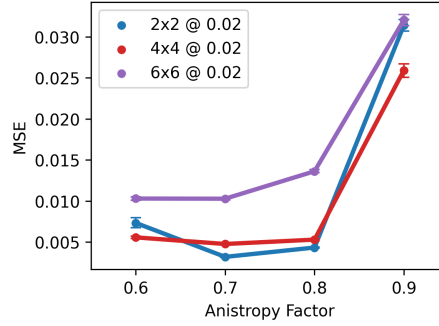

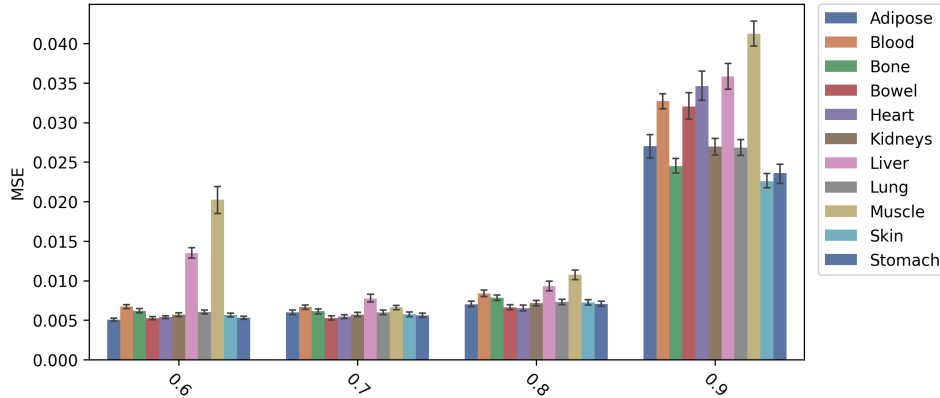**Figure 3.** Error of phase function estimation at different FOVs, averaged across all the tissues.

Figure 4. Error of phase function estimation for individual tissues, averaged across the FOVs in Figure 3.

Figure 4 shows the estimation error of individual tissues averaged across the above FOVs. When $g = 0.9$, the errors of all tissues are significantly larger compared to that at smaller values of g. At $g=0.6$, the errors of muscle and liver are significantly larger than that of other tissues. According to Table 1, these two tissues are low scattering tissues.

3.4. Effect of spatial resolution on estimation accuracy

Figure 5 shows the accuracy of phase function estimation on DS_2, DS_4 and DS_5, where the FOVs are fixed at 4×4 while the spatial resolutions are varied from 0.02 (DS_2) to 0.01 (DS_4) or 0.04 (DS_5). Based on the reference resolution of 0.02 (red dots), the estimation error increases by 65.5% (Table 3) when the resolution is increased to 0.01 (orange dots). When the resolution is reduced to 0.04 (green dots), the estimation error increases by 9.1% on average. The increment of the error comes from the large error at $g=0.9$. At other g values, the estimation errors at resolution 0.04 are smaller than those at resolution 0.02.
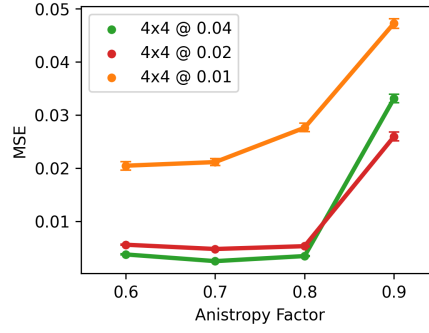

Figure 5. Error of phase function estimation at different spatial resolutions, averaged across all the tissues.
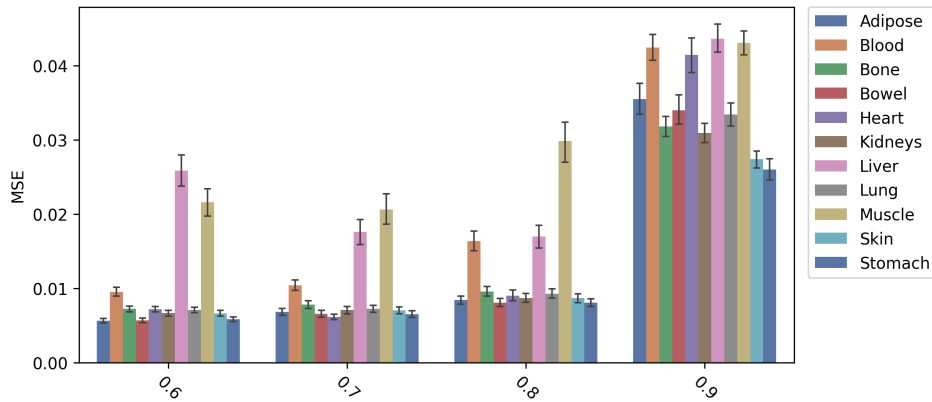

Figure 6. Error of phase function estimation for individual tissues, averaged across the resolutions in Figure 5.

Figure 6 shows the estimation error of individual tissues averaged across the different resolutions. Similar to the results in Figure 4, the errors are significantly larger at $g = 0.9$ compared to that at smaller values of g. At other g values, the three low scattering tissues, muscle, liver, and blood, have significantly higher errors than the other tissues.

4. Discussion

Some of the above experimental results seem to be somewhat unreasonable at first glance. For example, increasing the FOV and improving the spatial resolution are not only unhelpful but even harmful in some cases to improve the estimation accuracy. In general, we always want an imaging system to have as high a resolution as possible with a sufficient FOV to guarantee the measurement accuracy. To justify the results, we investigate the distribution of the reflectance signals and the similarity of the reflectance images for different tissues and anisotropy factors.
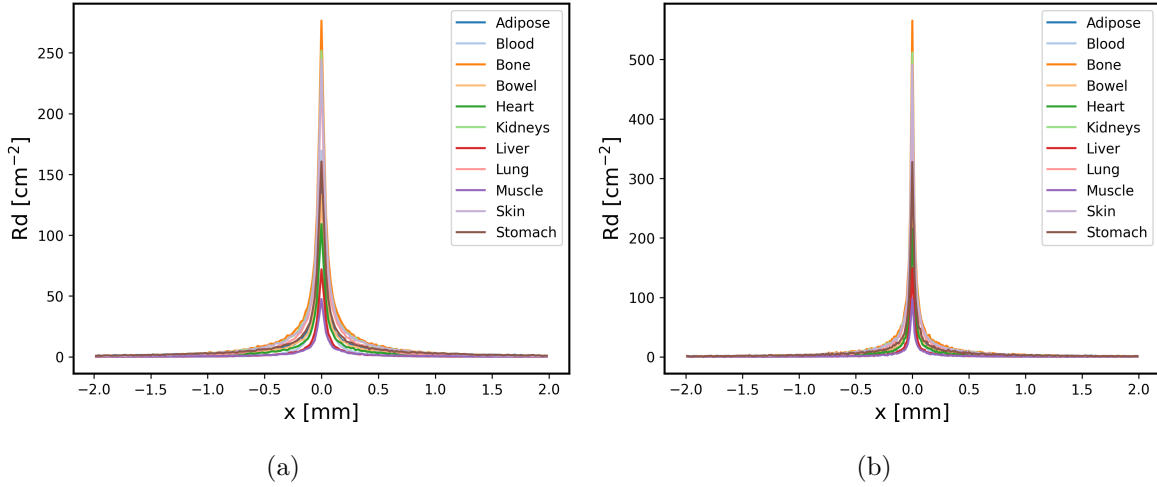

(a)   (b)

Figure 7. Profiles of test images. (a) DS_2, FOV=4×4@0.02. (b) DS_4. FOV=4×4@0.01. The anisotropy factor $g = 0.6$ for both sub-images.

4.1. Why expanding FOV not improving the estimation accuracy

Considering the radial symmetry of the reflectance images, the horizontal profiles through the incident points of the test images in DS_2 and DS_4 are shown in Figure 7. The profiles are extracted from the images with $g = 0.6$ because the stronger scattering makes it easier to observe the relationship of different tissues.

Since our experimental setup employs an infinitely narrow incident beam and does not consider the camera model, the obtained reflectance images are actually the ideal impulse response of different tissues sampled at different FOVs and spatial resolutions. Figure 7(a) shows the profiles at the FOV of 4×4 and the resolution of 0.02. It can

be seen that the reflectance signals are mainly concentrated in the range of [-1, 1] mm, corresponding to a FOV of 2×2 mm². The estimation errors are comparable for the FOVs of 2×2 and 4×4 (Figure 3), and it is a little better for FOV 4×4 on average (Table 3). This indicates that the region between FOV 2×2 and 4×4 has a certain level of discriminative ability despite the small difference in the amplitude of the reflectance signals. However, further increasing the FOV to 6×6, the estimation error increases significantly, as shown in Figure 3 and Table 3. We interpret the results to mean that as the FOV expands, the reflectance signals become less distinguishable in terms of amplitude and distribution.

As pointed in Bodenschatz et al. (2016), the further away photons are detected from the incident beam, the deeper they have penetrated into the tissues. The reflectance intensities far away from the incident point are contributed by the diffusive background, while the proximal intensities are composed of both the subdiffusive scattering and diffusive background. Since the diffusive background is weakly influenced by the scattering phase function, a more elaborate network design and more training samples may be required to take full advantage of it for phase function estimation.

4.2. Why increasing the spatial resolution conversely reducing the estimation accuracy

Figure 7(b) shows the profiles at the FOV of 4×4 and the resolution of 0.01. Compared with 7(a), the profiles have narrower lobes, larger amplitudes, and more clearly delineated fluctuations. This result is easy to interpret, since we use a higher spatial resolution to sample an ideal impulse response. However, the distances of different tissue profiles have also become smaller and even intersected, thus greatly increasing the difficulty for the PhaseNet models to discriminate different phase functions and leading to a significant increase in their estimation errors.

The increased fine details in the reflectance images with high spatial resolution suggest that the learning task becomes more difficult for PhaseNet. Without changing the network structure, a simple countermeasure is to increase the number of training samples. To verify this hypothesis, the number of training samples per parameter set in DS_4 is increased from 200 to 400, thus doubling the total number of training data. Five PhaseNet models are trained with the same hyperparameters as before and tested on the original test dataset of DS_4. The resulting MSE is 0.016±0.017 and the relative error of g is 4.201±3.805 %. The MSE is decreased by 44.8% after doubling the training data.

4.3. Why phase function with large g being difficult to learn

The results in Section 3 show that at g=0.9 (the largest value we tested), the estimation errors are significantly higher than that of other g values, regardless the FOV, resolution or tissue type. When the anisotropy factor is large, the propagation of light is dominated by forward-scattering. As a result, the reflectance image becomes more close to a two-dimensional impulse function than that of smaller g. This will require a higher spatial

resolution to delineate the reflectance distribution. In other words, the reflection image at large g values is more likely to be spatially undersampled.

4.4. Why the errors of muscle, liver and blood being large

Figure 4 and 6 show that in most cases the estimation errors are larger for muscle, liver and blood than for other tissues. All the three types of tissues are low scattering, as classified in Table 1. Low scattering means that more photons are forward scattered or absorbed as the light propagates in this type of tissue. This results in a lower intensity and smaller size spot in the reflectance images. As shown in Figure 7, the lowest amplitude and the smallest width of the profiles are found for muscle and liver. Similar to the case of large g values, the small main lobe width of the reflectance image can explain in one aspect why the estimation error of phase function is larger for low scattering tissues.

The representational similarity analysis (RSA) (Kriegeskorte et al.; 2008) is employed to analyze this issue in more depth. RSA is widely used in neuroscience to compare representations across domains by using the representational dissimilarity matrices (RDMs). The RDMs are square symmetric matrices with zero diagonal that encode the (dis)similarity between all pairs of data samples or conditions in a dataset. We compute the RDMs using Euclidean distance for two representations of the reflectance image, namely the profiles of the original image and the image features extracted by the PhaseNet model. The output of the global pooling layer in PhaseNet is used as the image feature. The resulting RDMs of DS_2 are shown in Figure 8. Since there are 1760 images (11 tissues, 4 g values, 40 samples per g value) in the test set, the size of the RDMs is 1760×1760 pixels. The images are sorted by tissue type first and then by g value.
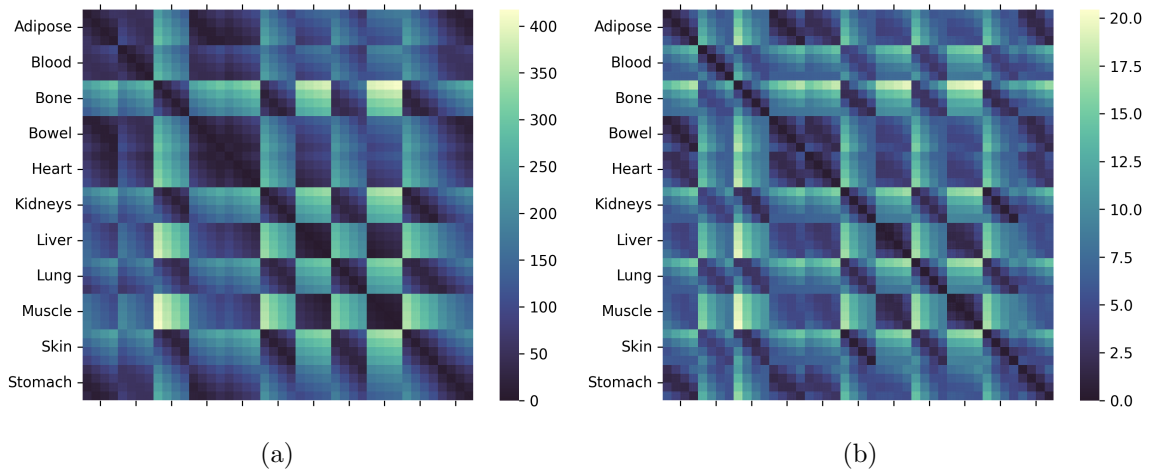

(a)   (b)

Figure 8. Representational dissimilarity matrices (RDMs) of the test images in DS_2. (a) RDM of the profiles of the original images. (b) RDM of the image features.

The RDMs in Figure 8 appear to be composed of small cells. The size of the cells is 40×40 pixels, demonstrating that the variation between images generated with same parameters (μ_a, μ_s and g) is small. A square of 4×4 cells indicates the degree to which each pair of tissues is distinguished, or the degree of differentiation of the same tissue with different g values when the square is on the diagonal. It can be seen that there are four large dark squares of size 8×8 cells in the top-left quarter of Figure 8(a), indicating that adipose, blood, bowel and heart are closer to each other. The closer relationship between bone, kidneys, lung and skin can also be observed. It is worth noting in particular the four dark squares corresponding with liver and muscle. They show not only that liver and muscle have similar reflectances, but also that it is difficult to distinguish between livers or muscles with different g values due to the homogeneity in the squares. Therefore, it is easy to understand why the estimation error of phase function for liver and muscle is larger than other tissues. As for blood, it has the largest absorption coefficient among the tissues used. Since a large amount of light is absorbed, the estimation error of the phase function is also larger for high absorption tissues. Our results are consistent with the findings of optical parameter estimation in (Hokr and Bixler; 2021).

In the RDM of the image features (Figure 8(b)), the dark square effect is significantly weakened and the heterogeneity of each square is remarkably increased. This shows a better discriminability between different tissues and different g values in the feature space.

4.5. Limitations

There are several limitations that should be noted when interpreting the results of this study. First, the experimental configuration does not consider the incident light beam form, the imaging system model and noise. The reflectance images are the ideal impulse response of tissues. Therefore, the FOV and resolution values in the experimental results are not applicable to a real imaging system. Second, the optimal number of Gaussian components for DS_2 is applied to all other datasets because we want the experimental factors other than FOV and resolution to be as consistent as possible. This may degrade the performance on these datasets. Third, since FOV, resolution and image size are interrelated, the image size of the datasets cannot be the same when varying the FOV and resolution. Comparing the PhaseNet models with different input image sizes is not fair, but only as a last resort, because we do not want to introduce interpolation errors by normalizing the image sizes.

5. Conclusion

In this study, we proposed to directly estimate the phase function form of the light propagation model from the diffuse reflectance images using convolutional neural networks. An analytic phase function representation scheme based on Gaussian mixture

model was presented for a modified ResNet-18 regression model. The proposed method was validated on MC simulated reflectance images of 11 biological tissues and HG phase function with different anisotropy factors. The results showed that the best mean-squared-error was 0.01 and the relative error of the anisotropy factor was 3.28%, demonstrating the feasibility and accuracy of using convolutional neural network as an inverse MC model. A comparative analysis of the effects of field of view and spatial resolution on estimation accuracy was conducted. The results suggest that the learning task becomes more difficult when the reflectance images contain more indistinguishable information or fine reflectance details, which requires more elaborate network model design and more training data.

Acknowledgments

References

Alerstam, E., Svensson, T. and Andersson-Engels, S. (2008). Parallel computing with graphics processing units for high-speed Monte Carlo simulation of photon migration, *Journal of Biomedical Optics* **13**(6): 1–3.

Alexandrakis, G., Rannou, F. R. and Chatziioannou, A. F. (2005). Tomographic bioluminescence imaging by use of a combined optical-PET (OPET) system: a computer simulation feasibility study, *Physics in Medicine and Biology* **50**(17): 4225–4241.

Bengio, Y., Lecun, Y. and Hinton, G. (2021). Deep learning for ai, *Communications of the ACM* **64**(7): 58–65.

Bevilacqua, F. and Depeursinge, C. (1999). Monte Carlo study of diffuse reflectance at source–detector separations close to one transport mean free path, *Journal of the Optical Society of America A* **16**(12): 2935–2945.

Bishop, C. (2006). *Pattern Recognition and Machine Learning*, Springer.

Bodenschatz, N., Krauter, P., Liemert, A. and Kienle, A. (2016). Quantifying phase function influence in subdiffusively backscattered light, *Journal of Biomedical Optics* **21**(3): 1–11.

Bodenschatz, N., Krauter, P., Nothelfer, S., Foschum, F., Bergmann, F., Liemert, A. and Kienle, A. (2015). Detecting structural information of scatterers using spatial frequency domain imaging, *Journal of Biomedical Optics* **20**(11): 1 – 7.

Calabro, K. W. and Bigio, I. J. (2014). Influence of the phase function in generalized diffuse reflectance models: review of current formalisms and novel observations, *Journal of Biomedical Optics* **19**(7): 1 – 15.

Chen, X., Yang, D., Sun, F., Cao, X. and Liang, J. (2016). Adaptively alternative light-transport-model-based three-dimensional optical imaging for longitudinal and

quantitative monitoring of gastric cancer in live animal, *IEEE Transactions on Biomedical Engineering* **63**(10): 2095–2107.

Cheong, W., Prahl, S. and Welch, A. (1990). A review of the optical properties of biological tissues, *IEEE Journal of Quantum Electronics* **26**(12): 2166–2185.

Fang, Q. and Boas, D. A. (2009). Monte Carlo simulation of photon migration in 3D turbid media accelerated by graphics processing units, *Optics Express* **17**(22): 20178–20190.

Goda, K., Jalali, B., Lei, C., Situ, G. and Westbrook, P. (2020). AI boosts photonics and vice versa, *APL Photonics* **5**(7): 070401.

He, K., Zhang, X., Ren, S. and Sun, J. (2016). Deep residual learning for image recognition, *2016 Computer Vision and Pattern Recognition*, IEEE, pp. 770–778.

Henyey, L. G. and Greenstein, J. L. (1941). Diffuse radiation in the Galaxy., *Astrophysical Journal* **93**: 70–83.

Hokr, B. H. and Bixler, J. N. (2021). Machine learning estimation of tissue optical properties, *Scientific Reports* **11**: 6561.

Ishimaru, A. (1978). *Wave Propagation and Scattering in Random Media*, Vol. 1, Academic Press New York.

Ivančič, M., Naglič, P., Pernuš, F., Likar, B. and Bürmen, M. (2018). Efficient estimation of subdiffusive optical parameters in real time from spatially resolved reflectance by artificial neural networks, *Optics Letters* **43**(12): 2901–2904.

Jacques, S. L. (2013). Optical properties of biological tissues: a review, *Physics in Medicine and Biology* **58**(11): R37–R61.

Klose, A. D. and Larsen, E. W. (2006). Light transport in biological tissue based on the simplified spherical harmonics equations, *Journal of Computational Physics* **220**(1): 441–470.

Kriegeskorte, N., Mur, M. and Bandettini, P. (2008). Representational similarity analysis - connecting the branches of systems neuroscience, *Frontiers in Systems Neuroscience* **2**: 4.

Naglič, P., Zelinskyi, Y., Likar, B., Pernuš, F. and Bürmen, M. (2019). From Monte Carlo simulations to efficient estimation of optical properties for spatial frequency domain imaging, *in* B. W. Pogue and S. Gioux (eds), *Molecular-Guided Surgery: Molecules, Devices, and Applications V*, Vol. 10862, International Society for Optics and Photonics, SPIE, pp. 8–15.

Naglič, P., Pernuš, F., Likar, B. and Bürmen, M. (2017). Lookup table-based sampling of the phase function for monte carlo simulations of light propagation in turbid media, *Biomedical Optics Express* **8**(3): 1895–1910.

Periyasamy, V. and Pramanik, M. (2017). Advances in Monte Carlo simulation for light propagation in tissue, *IEEE Reviews in Biomedical Engineering* **10**: 122–135.

Ren, S., Chen, X., Wang, H., Qu, X., Wang, G., Liang, J. and Tian, J. (2013). Molecular Optical Simulation Environment (MOSE): A platform for the simulation of light propagation in turbid media, *PLoS ONE* **8**(4): e61304.

Rowland, R., Ponticorvo, A., Lopez, A. J., Li, S., Li, X., Ichii, H. and Durkin, A. J. (2019). Monitoring kidney optical properties during cold storage preservation with spatial frequency domain imaging, *Journal of Biomedical Optics* **24**(11): 1 – 7.

Sun, Z., Xie, L., Hu, D. and Ying, Y. (2021). An artificial neural network model for accurate and efficient optical property mapping from spatial-frequency domain images, *Computers and Electronics in Agriculture* **188**: 106340.

Wang, G., Zhang, Y., Ye, X. and Mou, X. (2020). *Machine Learning for Tomographic Imaging*, IOP Publishing.

Wang, L., Jacques, S. L. and Zheng, L. (1995). MCML–Monte Carlo modeling of light transport in multi-layered tissues, *Computer Methods and Programs in Biomedicine* **47**(2): 131–146.

Wang, L. V. and Wu, H. (2007). *Biomedical Optics: Principles and Imaging*, Wiley.

Wilson, B. C. (1995). Measurement of tissue optical properties: methods and theories, *in* A. J. Welch and M. J. C. Van Gemert (eds), *Optical-Thermal Response of Laser-Irradiated Tissue*, Springer US, Boston, MA, pp. 233–303.

Yaroslavsky, A. N., Yaroslavsky, I. V., Goldbach, T. and M.D., H.-J. S. (1999). Influence of the scattering phase function approximation on the optical properties of blood determined from the integrating sphere measurements, *Journal of Biomedical Optics* **4**(1): 47–53.

Zhao, Y., Deng, Y., Bao, F., Peterson, H., Istfan, R. and Roblyer, D. (2018). Deep learning model for ultrafast multifrequency optical property extractions for spatial frequency domain imaging, *Optics Letters* **43**(22): 5669–5672.